

Journal of Biomedical Optics

SPIEDigitalLibrary.org/jbo

Intravascular photoacoustic imaging at 35 and 80 MHz

Xiang Li
Wei Wei
Qifa Zhou
K. Kirk Shung
Zhongping Chen



SPIE

Intravascular photoacoustic imaging at 35 and 80 MHz

Xiang Li,^{a*} Wei Wei,^{b,c*} Qifa Zhou,^a K. Kirk Shung,^a and Zhongping Chen^{b,d,e}

^aUniversity of Southern California, Department of Biomedical Engineering, NIH Ultrasonic Transducer Resource Center, Los Angeles, California 90089

^bUniversity of California, Irvine, Beckman Laser Institute, Irvine, California 92612

^cWuhan University, Department of Physics and Key Laboratory of Acoustic and Photonic Materials and Devices, Wuhan 430072, China

^dUniversity of California, Irvine, Department of Biomedical Engineering, Irvine, California 92697

^eUniversity of California, Irvine, Edwards Lifesciences Center for Advanced Cardiovascular Technology, Irvine, California 92697

Abstract. The catheter-based intravascular photoacoustic (IVPA) imaging for diagnosing atherosclerosis, which can provide optical absorption contrast of the arterial wall besides acoustic scattering contrast from the conventional intravascular ultrasound (IVUS) imaging, has been intensively researched recently. The resolution of IVPA is determined by the frequency bandwidth of an ultrasonic transducer. Higher resolution can be achieved by increasing the transducer's working frequency and bandwidth. We introduce IVPA imaging at 35 and 80 MHz by using newly designed integrated IVUS/IVPA probes. This is the first time IVPA has been achieved as high as 80 MHz. Six-micrometer tungsten wires were imaged to evaluate the probes' spatial resolutions and beam patterns. Healthy rabbit aorta was imaged *in vitro*. Imaging results show that IVPA has superior contrast over IVUS in identifying the arterial wall, and IVPA at 80 MHz demonstrates extraordinary resolution (35 μm) compared to 35 MHz. © 2012 Society of Photo-Optical Instrumentation Engineers (SPIE). [DOI: [10.1117/1.JBO.17.10.106005](https://doi.org/10.1117/1.JBO.17.10.106005)]

Keywords: intravascular photoacoustic; intravascular ultrasound; high frequency; 80 MHz.

Paper JBO-12058 received Feb. 5, 2012; revised manuscript received Sep. 1, 2012; accepted for publication Sep. 7, 2012; published online Oct. 1, 2012.

1 Introduction

Coronary artery disease (CAD) is a complex syndrome characterized by plaques built up in the inner lining of coronary arteries, which is the number one killer of both men and women in the United States.¹ It has been shown that the rupture of vulnerable plaque, which is characterized by a thin fibrous cap and underlying necrotic core, is the major cause of luminal thrombosis in acute coronary syndrome (ACS).²⁻⁴ The conventional method for diagnosing the vulnerability of plaque is 20- to 40-MHz intravascular ultrasound (IVUS) imaging, which is capable of visualizing the structure of the vessel wall with large penetration depth and moderate resolution. IVUS can resolve certain plaques and lipid pools; however, the image contrast might be insufficient to distinguish the complex constituents in vulnerable plaque.⁵⁻⁷ Intravascular optical coherence tomography (OCT) possesses superior resolution and is useful for detecting microstructures, such as thin fibrous cap and endothelium. However, the major limitation of OCT is the shallow penetration depth, which is around 1 to 2 mm.⁷⁻¹¹

Intravascular photoacoustic (IVPA) imaging is a newly developed catheter-based, optical-acoustic hybrid modality, which is capable of providing optical absorption mapping of the arterial wall, offering not only morphological but also functional information.¹²⁻¹⁵ From transient laser irradiation on biological tissues, electromagnetic waves are absorbed and transient thermal expansion of the irradiated tissue is followed. As a result, broad band ultrasonic waves are generated and can be

received by an ultrasonic transducer. The ultrasonic signal strength is proportional to the absorbed optical energy in tissues.^{16,17} Recent studies have demonstrated the capability of spectroscopic IVPA imaging in detecting lipid,^{15,18,19} fibrous plaque,²⁰ and gold nanoparticle contrast agents.²¹ The *in vivo* study on rabbit has demonstrated the feasibility of applying IVPA without luminal blood clearance, which shows great potential for IVPA in clinical use.¹⁹ Most of the aforementioned researches were conducted with 40-MHz ultrasonic transducers. The imaging resolution is inversely proportional to the frequency bandwidth of the transducers. Higher center frequency and broader bandwidth transducers can provide better image resolutions.¹⁷ Our group has demonstrated the feasibility and improved resolution of applying 80-MHz ultrasonic transducers with IVUS imaging.²² However, IVPA imaging at 80 MHz has not been investigated. The improved resolution provided by 80 MHz IVPA could be beneficial in detecting certain atherosclerotic features.

For IVPA application, usually unfocused light pulses are delivered to illuminate the vessel wall. Researchers in prior studies used free space light shining from the outside of the vessel for *in vitro* experiments.^{13,14} More recently, integrated IVUS/IVPA catheters that can be used inside the vessel lumen have been extensively investigated. The design of the integrated IVUS/IVPA catheter normally incorporates an optical fiber for light delivery and an ultrasonic transducer for acoustic wave transmitting and receiving. Hsieh et al.²³ reported an integrated scan head incorporating a microring, cone-shaped mirror, and ring-shaped transducer. Wei et al.²⁴ reported an integrated probe with a concentrically arranged fiber and ring ultrasonic transducer. Jansen et al.¹⁵ and Karpouk et al.²⁵ reported a design of a sequentially arranged fiber and transducer. This design has an outer diameter of 1.2 mm, which is currently the smallest

*These authors contributed equally to this work.

Address all correspondence to: Qifa Zhou, University of Southern California, NIH Ultrasonic Transducer Resource Center, 1042 Downey Way, University Park, Los Angeles, California 90089. Tel: 213-740-9475; Fax: 213-821-3897; E-mail: qifazhou@usc.edu; Zhongping Chen, University of California, Irvine, Beckman Laser Institute, 1002 Health Sciences Road East, Irvine, California 92612. Tel: 949-824-1247; Fax: 949-824-8413; E-mail: z2chen@uci.edu.

version. In their reports, the optical and acoustic centers are separated by around 1 mm.

In this report, we present miniature integrated IVUS/IVPA probes with a parallel arranged optical fiber and ultrasonic transducer. Thirty-five— and 80-MHz ultrasonic transducers have been incorporated into the probes. The spatial resolutions and beam patterns of the probes were characterized. Healthy rabbit aorta was imaged *in vitro* with both 35- and 80-MHz IVUS/IVPA probes to investigate their capability for intravascular imaging.

2 Materials and Methods

The integrated IVUS/IVPA probe is composed of a parallel arranged, side-firing optical probe and side-viewing ultrasonic transducer, shown in Fig. 1. For the optical part, a 200- μm -core multimode fiber is used to deliver the 532 nm pulsed laser beams. At the distal end, a 45-deg polished microprism ($0.25 \times 0.25 \times 2 \text{ mm}^3$; Bern Optics Inc., Westfield, MA) is connected to the fiber tip and sealed inside a glass capillary tube (0.4 mm inside diameter; 0.55 mm outside diameter). Air is trapped inside the tube to form an air/glass interface at the prism polished surface to redirect laser beams by 90 deg, following the “total internal reflection” effects.^{15,25} The light divergence is measured to be 32 deg. For the acoustic part, 35- and 80-MHz ultrasonic transducers were fabricated in our laboratory²² and assembled into the IVUS/IVPA probes, respectively. In the 35-MHz transducer, a $[\text{Pb}(\text{Mg}_{1/3}\text{Nb}_{2/3})\text{O}_3]_{0.63}[\text{PbTiO}_3]_{0.37}$ (PMN-PT) crystal (HC Materials, Bolingbrook, IL) is used as the active piezoelectric element with a thickness of 55 μm and an aperture size of $0.4 \times 0.4 \text{ mm}^2$. To improve the performance of the transducer, a two-layer acoustic matching scheme is applied. The first matching layer is 16 μm silver-powder-loaded epoxy, and the second matching layer is 14 μm vapor-deposited parylene. In the 80-MHz transducer, the PMN-PT free-standing film, which is fabricated from a tape-casting method, is used as the piezoelectric layer with a thickness of 30 μm and the same aperture size as the 35-MHz transducer. The same two-layer matching scheme is applied to the 80-MHz transducer but with a thickness of 4.4 μm (first matching) and 1.8 μm (second matching). The -6 dB bandwidth of the 35-MHz transducer is 50% (26.5 to 44 MHz) and that of the 80-MHz transducer is 45% (62 to 98 MHz), which are determined from ultrasound pulse echo tests. The optical probe and ultrasonic transducer are fixed side by side inside the catheter. The centers of the optical and acoustic parts have a separation of around 0.5 mm. All components are packaged in polyimide tubing (Small Parts, Inc., Miramar, FL) with 1.2 mm OD. The optical and acoustic

beams are aligned to have an angle of approximately 20 deg to achieve optimal overlapping. The overall size of the probe is comparable to the probes reported by Karpouk et al.²⁵ and Jansen et al.¹⁵ However, the separation between the optical and acoustic elements are smaller than in the prior design. The closer arrangement may improve the optical—acoustic overlapping, especially at the region close to the probe surface. By incorporating either 35- or 80-MHz ultrasonic transducers, we fabricated the integrated IVUS/IVPA probes working at each frequency range.

In the IVPA system, a pulsed Q-switched Nd:YAG laser (532 nm, 3 ns pulse width, 10 Hz repetition rate; Continuum, Inc., Santa Clara, CA) is used as the excitation source. The free space laser output is coupled by a 4 \times objective lens into an optical fiber, which is then delivered to the prism at the distal end of the integrated IVUS/IVPA probe. The probe is inserted into the vessel lumen and internally illuminates the vessel wall with a laser energy of 0.9 to 1 mJ/pulse. Circumferential scanning is achieved by rotating a water tank with the specimen inside using a stepper motor while the probe is kept immobile. A PR5900 pulser/receiver (Olympus NDT, Inc., Kennewick, WA) is used to generate ultrasound pulses and receive both ultrasound and photoacoustic waves. Received signals are digitized and processed in the computer. For each IVPA scan, 1000 A-lines are acquired and averaged by every two A-lines to reduce noise. All A-lines are digitally band-pass filtered according to the transducer’s bandwidth. After envelope detection, the A-lines are scan converted into radial format for display. The IVUS scan is then followed with the same scanning pattern at the same cross section. Co-registration between IVUS and IVPA is ensured by the precision of motor stepping. The scanning procedure is controlled by a custom-built LabVIEW program (National Instruments, Austin, TX) and synchronized by laser trigger signals.

The resolution of both 35- and 80-MHz probes in IVPA imaging is measured by linearly scanning a wire phantom along the transversal direction. The wire phantom is composed of three 6- μm -OD tungsten wires which are separated by 1.5 mm in the axial direction and 0.65 mm in the lateral direction. Moreover, in order to characterize the beam pattern of the IVPA probes when doing rotational movement, a series of images are acquired by rotating one tungsten wire 360 deg at different depths along the radial direction. The wire images are fused into one image to depict the beam pattern.

To evaluate the capability of the integrated IVUS/IVPA probes in intravascular imaging, *in vitro* experiments have been conducted at both 35 and 80 MHz. A section of healthy rabbit abdominal aorta was harvested and preserved in phosphate buffer. During the experiment, the specimen was immersed and supported by a sponge to stand in a water tank. Only the part of specimen above the sponge was imaged. The imaged sections were pinpointed for hematoxylin-eosin (H&E)-stained histology examination.

3 Results and Discussion

The photoacoustic images of the 6- μm wire targets at 35 and 80 MHz are shown in Figs. 2(a) and 3(a), respectively. The dynamic ranges of the two images are 30 dB. Figures 2(b) and 3(b) show the envelopes of the photoacoustic signals from the wire located around 2.5 mm away from the probe surface. Axial and lateral resolutions are determined from the -6 dB envelope width, which are 59 and 232 μm at 35 MHz; 35 and 181 μm at 80 MHz. The RF signals and spectra

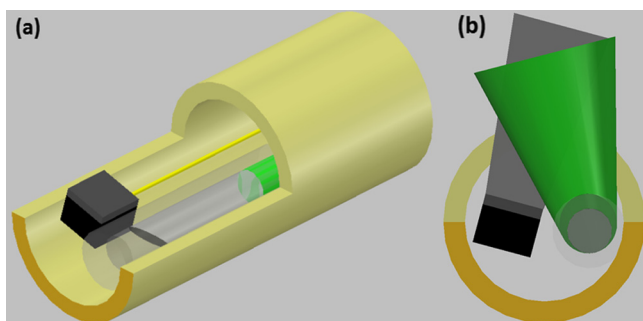


Fig. 1 Schematic of the integrated IVUS/IVPA probe: top view (a) and front view (b); the light beam is in green and the acoustic beam in gray.

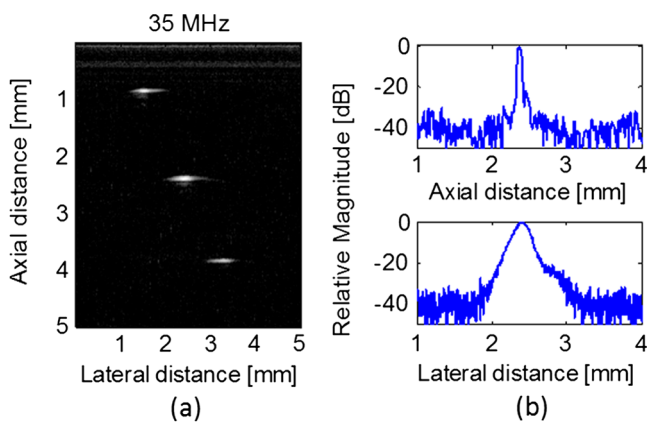


Fig. 2 Thirty-five-MHz photoacoustic image of 6- μ m tungsten wires (a), displayed with 30 dB dynamic range; axial and lateral envelopes (b) of the photoacoustic signal from the wire located 2.5 mm away from the transducer surface.

of photoacoustic signals generated by the wire targets at 35 and 80 MHz are shown in Fig. 4(a) and 4(b), respectively. The pulse width at 80 MHz is roughly half of the length at 35 MHz, which explains the improved axial resolution at 80 MHz. As shown in Fig. 4, the peak center frequencies of the photoacoustic spectra are 35 and 80 MHz, which is similar to the ultrasound pulse echo test results. The -6 dB bandwidth of the 35-MHz photoacoustic signal is measured to be 19 to 45.5 MHz, which indicates an effective center frequency of 32 MHz and a fractional bandwidth of 83%. The -6 dB bandwidth of the 80-MHz photoacoustic signal is measured to be 35 to 107 MHz, which indicates an effective center frequency of 71 MHz and a fractional bandwidth of 102%. Compared to the ultrasound pulse echo test results, the bandwidths of the photoacoustic signals at both 35 and 80 MHz broadened. It can be explained by the broadband nature of the photoacoustic signals and the lack of a transmitting narrowing effect which only happens to ultrasound pulse echo signals. The downshifting of an effective center frequency is probably caused by the relatively stronger photoacoustic signals at lower frequencies. The effects of bandwidth increase and center frequency downshift are consistent with the findings reported at 40 MHz by Sethuraman et al.¹³

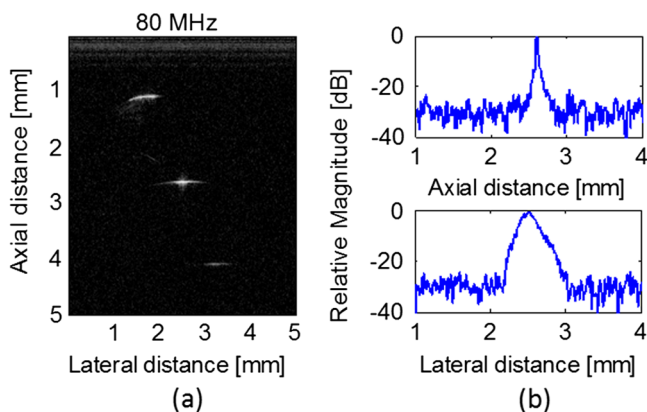


Fig. 3 Eighty-MHz photoacoustic image of 6- μ m tungsten wires (a), displayed with 30 dB dynamic range; axial and lateral envelopes (b) of the photoacoustic signal from the wire located 2.5 mm away from the transducer surface.

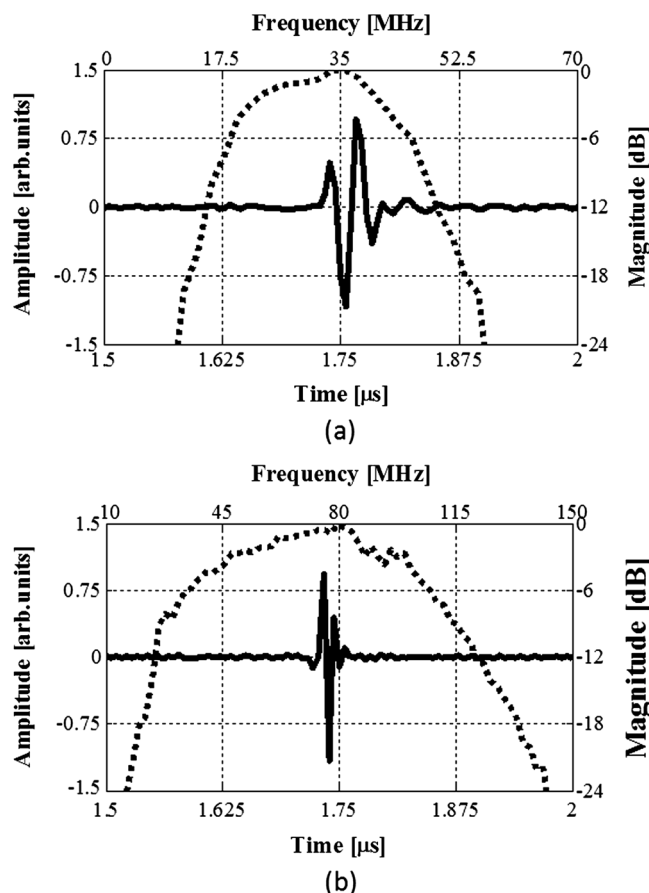


Fig. 4 Photoacoustic signals and spectra generated by a wire target at 35 MHz (a) and 80 MHz (b); the wire is located at a depth of 2.5 mm.

The beam patterns of the photoacoustic signals are demonstrated in Fig. 5. During the imaging, one tungsten wire is positioned at depths from 0.5 to 5 mm along the radial direction with 0.5 mm increments. At each depth, a 360-deg radial format image is acquired at both 35 and 80 MHz. After acquiring images at all depths for each frequency, they are fused into one image for display. Figure 5(a) and 5(b) shows the scan converted images in Cartesian coordinates at 35 and 80 MHz, respectively, with a dynamic range of 30 dB. The

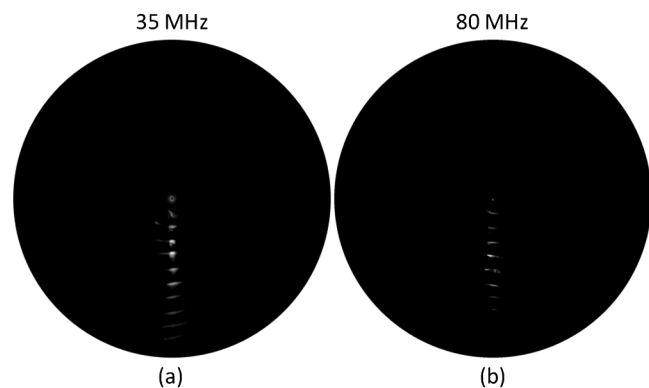


Fig. 5 Wire phantom photoacoustic images in Cartesian coordinates show the photoacoustic beam pattern at 35 MHz (a) and 80 MHz (b). The wires in the images are separated by 0.5 mm. The image is displayed with a 30-dB dynamic range and covers a radial distance of 5.5 mm.

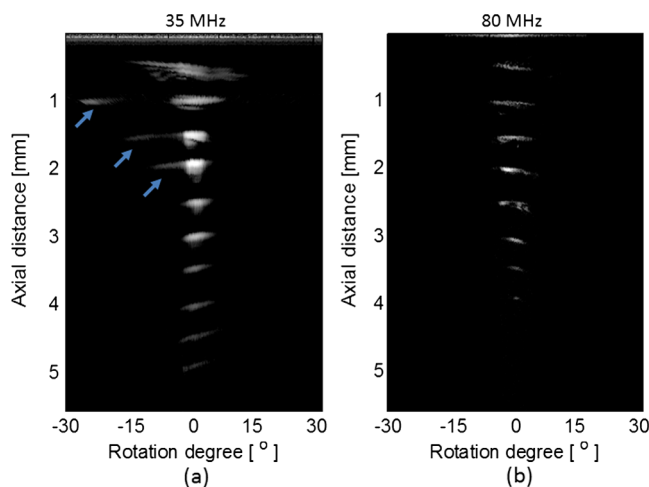


Fig. 6 The same wire phantom photoacoustic images as shown in Fig. 5 but displayed in polar coordinates. Both the 35-MHz (a) and 80-MHz (b) images cover an angular range from -30 deg to $+30$ deg. The blue arrows in (a) indicate side lobes.

images cover a radial distance of 5.5 mm. In both 35- and 80-MHz images, beams become broader as they travel from a longer distance to the probe. The beam patterns are presented in Fig. 6, which is a zoomed-in version of Fig. 5 in the polar coordinates and covers an angular range from -30 deg to $+30$ deg. The maximum amplitudes of the wire photoacoustic signals at each depth are plotted in Fig. 7. The highest amplitudes are found at 2 mm in both the 35- and 80-MHz images, which indicates the optimal optical–acoustic overlap distance. The lateral resolutions measured at this depth are 3.21 deg for the 35-MHz probe and 3.18 deg for the 80-MHz probe. In the 35-MHz image, the farthest detectable wire is located as far as 5 mm; while in the 80-MHz image, the farthest detectable depth is 4 mm. The shorter detectable distance at 80 MHz is caused by the higher attenuation of

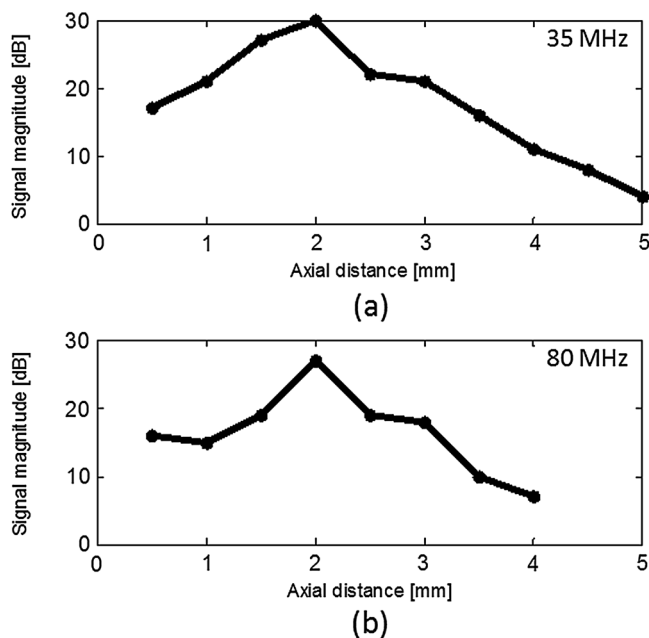


Fig. 7 Plot of the maximum amplitudes of the wire photoacoustic signals versus axial distance at 35 MHz (a) and 80 MHz (b).

acoustic energy at 80 MHz. Due to the same reason, beams in the 80-MHz image become relatively narrower after 3 mm. However, the farthest detectable wire may not necessarily represent the farthest optical–acoustic overlapping depth because the $6\text{-}\mu\text{m}$ tungsten wire is very thin and relatively weak in echogenicity. In another test in which a $500\text{-}\mu\text{m}$ pencil was used as the target, both 35- and 80-MHz probes could image the target more than 5 mm away.

In the 35-MHz photoacoustic image, side lobes are observed for wires located at a depth from 1 to 2 mm, which are indicated by blue arrows in Fig. 6(a). The side lobes are caused by the non-concentric arrangement of optical and acoustic beams. The side lobes only occur on the side at which optical element is placed, where the light fluence is relatively stronger than the other side. The side lobes may not significantly affect the imaging quality because the amplitudes of the side lobes are 15 to 20 dB lower than the main lobes. The strength of the side lobes depends on optical–acoustic alignment, light fluence strength, and ultrasonic transducer sensitivity. Although the side lobes are undesirable, they could happen to all non-concentrically aligned optical and acoustic beams. In the sequentially arranged designs, the side lobes could be manifest along the longitudinal direction, on the optical element side.

By using the integrated IVUS/IVPA probes, *in vitro* imaging of a normal rabbit aorta was conducted at both 35 and 80 MHz to demonstrate the probes' imaging feasibility. IVUS and IVPA images of a rabbit aorta at 35 MHz are shown in Fig. 8(a) and 8(b). The IVUS image has a dynamic range of 50 dB, and the IVPA image has a dynamic range of 35 dB. Both images can be seen through the vessel wall. The 35 MHz IVPA imaging depth could be demonstrated up to 4 mm at the 12:00 to 2:00 o'clock position in Fig. 8(b). The aorta vessel wall is composed of three-layer structures: intima, media, and adventitia. Intimal thickening is considered to be a manifestation of atherosclerosis.²⁶ Since the aorta used in this study is from a healthy rabbit,

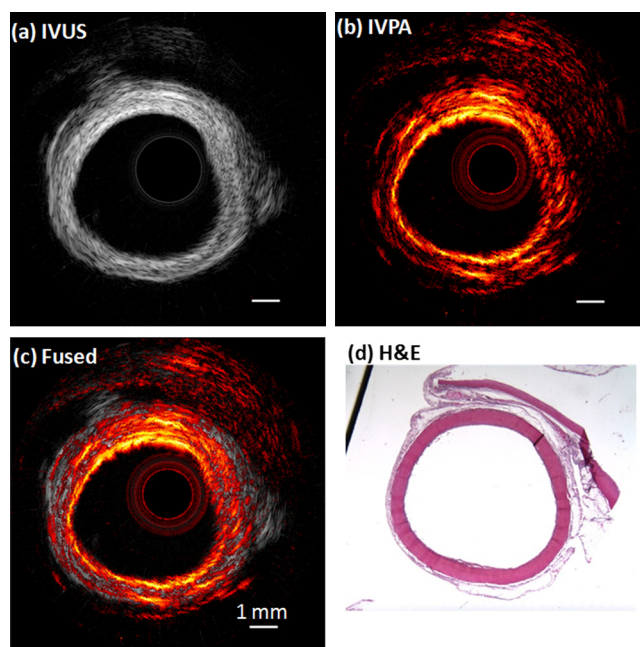


Fig. 8 Cross-sectional IVUS (a), IVPA (b), and fused (c) images of a healthy rabbit aorta at 35 MHz, and hematoxylin-eosin (H&E)-stained histology image (d). The IVUS image is displayed with 50 dB dynamic range, and the IVPA image is displayed with 35 dB dynamic range.

the intima only displays as a very thin darker layer in the histology image, and the vessel wall has a relatively uniform composition, as shown in Fig. 8(d). Therefore, it is not surprising that the IVUS and IVPA images have a relatively homogeneous appearance. In the IVPA image, due to the boundary buildup effect,²⁷ the front and rear boundaries are more prominent than the middle. Figure 8(c) shows the fused IVUS/IVPA image, which demonstrates the coregistration of the two images.

The 80-MHz IVUS and IVPA images are shown in Fig. 9(a) and 9(b). The IVUS image has a dynamic range of 50 dB, and the IVPA image has a dynamic range of 35 dB. Due to the improved axial resolution at 80 MHz, the profile of the vessel lumen is depicted more clearly in both IVUS and IVPA images than at 35 MHz. In the 80-MHz IVUS image, as shown in Fig. 9(a), owing to the insufficient acoustic contrast between adventitia and soft tissue surrounding the aorta, the outer boundary of the vessel wall is not clearly displayed, especially from the 8:00 to 2:00 o'clock position, while in the IVPA image, as shown in Fig. 9(b), the outer boundary is more evident. By fusing the IVUS and IVPA images together, as shown in Fig. 9(c), the boundary between surrounding soft tissue and vessel wall can be easily seen. Compared to the 35-MHz IVPA image, the 80-MHz image displays a clearer boundary profile of the vessel wall, which demonstrates improved axial resolution at a higher frequency.

During the study, the vessel was illuminated from inside by a 532-nm laser light; hence, the inner part of the vessel received stronger irradiation, which may have resulted in a brighter appearance for the lumen boundary in the IVPA image. On the other hand, the vessel is majorly occupied by the media layer, which is composed of smooth muscle cells. The smooth muscle cells also act as micro-absorbers and scatterers, which generate a homogenous appearance of the vessel wall in the IVUS image but build up boundaries of the vessel wall in

the IVPA image. The boundary buildup effect²⁷ is briefly explained as follows. In a slab of tissue, cells act as a collection of randomly distributed sub-resolution absorbers and scatterers. The photoacoustic waves emitted from these absorbers interfere with each other. Since optical absorbers expand on laser excitation, all initial photoacoustic pressure increases are positive. The detected photoacoustic waves from the absorbers close to the boundaries are approximately equal in phase delay and thus add constructively to manifest the boundaries. On the other hand, photoacoustic waves from the central absorbers have completely randomized phases which result in the cancellation of each other. Therefore, prominent boundary photoacoustic signals of the vessel wall are observed while the random fluctuations in the middle are suppressed. The length of the boundary signal is affected by the ultrasonic wavelength. Thus, the boundary in the 80-MHz IVPA image looks thinner and more evident than that in the 35-MHz image. In other words, the 35-MHz IVPA image looks more homogeneous.

Luminal blood is a major limitation for IVPA applications. Hemoglobin and oxyhemoglobin have higher optical absorption rates than arterial wall constituents at the wavelength range of 500 to 600 nm.²⁸ In this range, blood will absorb most of the light and feed back strong photoacoustic responses. Moreover, the blood attenuation and backscattering effects on ultrasonic waves becomes stronger when the frequency goes beyond 65 MHz.²⁹ The backscattering effects could degrade imaging contrast between blood and vessel and limit the ultrasound's ability to see through blood and even further reduce the penetration depth in the vessel wall. Therefore, for IVPA in *in vivo* experiments and clinical use, techniques such as flushing and balloon occlusion used in intravascular OCT could be adapted to reduce the blood interference. We have successfully demonstrated a new IVUS/IVPA probe design and the feasibility of applying IVPA at 35 and 80 MHz at a wavelength of 532 nm. The 532-nm light is useful in detecting fibrocellular inflammatory plaque and provides extrinsic contrast using the gold nanoparticle as a contrast agent.^{14,21} However, the probes could be easily transferred for multispectral IVPA applications using the NIR wavelength excitation.

4 Conclusion

In summary, we have introduced miniature integrated IVUS/IVPA probes that could internally illuminate the vessel wall and provide IVUS and IVPA imaging simultaneously. The optical and acoustic components were arranged parallel to each other. Thirty-five- and 80 MHz ultrasonic transducers were incorporated into the integrated probes to perform IVPA imaging at each frequency. *In vitro* wire phantom and rabbit aorta experiments were successfully conducted to verify the feasibility of applying these probes for intravascular imaging. Compared to the 35-MHz IVPA imaging, the 80-MHz IVPA imaging demonstrated much finer resolution for delineating vessel boundaries.

Acknowledgments

This project was supported by grants from the National Institutes of Health (EB-10090, RR-01192, EB-00293, P41-EB2182). Wei Wei was supported in part by the China Scholarship Council (CSC). Xiang Li was supported in part by a USC Provost Fellowship.

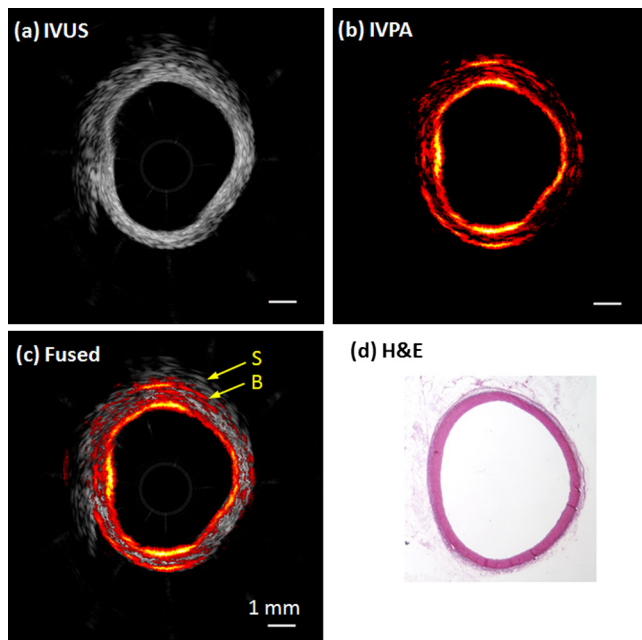


Fig. 9 Cross-sectional IVUS (a), IVPA (b), and fused (c) images of a healthy rabbit aorta at 80 MHz, and H&E-stained histology image (d). The IVUS image is displayed with 50 dB dynamic range, and the IVPA image is displayed with 35 dB dynamic range. S: surrounding soft tissue; B: boundary between vessel wall and surrounding soft tissue.

References

1. National Heart Lung and Blood Institute, "What is atherosclerosis?," <http://www.nhlbi.nih.gov/health/health-topics/topics/atherosclerosis/> (19 September 2012).
2. M. J. Davies and A. Thomas, "Thrombosis and acute coronary-artery lesions in sudden cardiac ischemic death," *N. Engl. J. Med.* **310**(18), 1137–1140 (1984).
3. R. Virmani et al., "Lessons from sudden coronary death: a comprehensive morphological classification scheme for atherosclerotic lesions," *Arterioscler. Thromb. Vasc. Bio.* **20**(5), 1262–1275 (2000).
4. R. Virmani et al., "Atherosclerotic plaque progression and vulnerability to rupture," *Arterioscler. Thromb. Vasc. Bio.* **25**(10), 2054–2061 (2005).
5. G. Pasterkamp et al., "Techniques characterizing the coronary atherosclerotic plaque: influence on clinical decision making," *J. Am. Coll. Cardiol.* **36**(1), 13–21 (2000).
6. F. S. Foster et al., "Advances in ultrasound biomicroscopy," *Ultrasound Med. Biol.* **26**(1), 1–27 (2000).
7. T. Sawada et al., "Feasibility of combined use of intravascular ultrasound radiofrequency data analysis and optical coherence tomography for detecting thin-cap fibroatheroma," *Eur. Heart J.* **29**(9), 1136–1146 (2008).
8. R. Puri, M. I. Worthley, and S. J. Nicholls, "Intravascular imaging of vulnerable coronary plaque: current and future concepts," *Nat. Rev. Cardiol.* **8**(3), 131–139 (2011).
9. P. Patwari et al., "Assessment of coronary plaque with optical coherence tomography and high-frequency ultrasound," *Am. J. Cardiol.* **85**(5), 641–644 (2000).
10. J. Yin et al., "Novel combined miniature optical coherence tomography ultrasound probe for in vivo intravascular imaging," *J. Biomed. Opt.* **16**(6), 060505 (2011).
11. X. Li et al., "High-resolution coregistered intravascular imaging with integrated ultrasound and optical coherence tomography probe," *Appl. Phys. Lett.* **97**(13), 133702 (2010).
12. B. Wang et al., "Intravascular photoacoustic imaging," *IEEE J. Quantum. Electron.* **16**(3), 588–599 (2010).
13. S. Sethuraman et al., "Intravascular photoacoustic imaging using an IVUS imaging catheter," *IEEE Trans. Ultrason. Ferroelectr. Freq. Control* **54**(5), 978–986 (2007).
14. S. Sethuraman et al., "Ex vivo characterization of atherosclerosis using intravascular photoacoustic imaging," *Opt. Express* **15**(25), 16657–16666 (2007).
15. K. Jansen et al., "Intravascular photoacoustic imaging of human coronary atherosclerosis," *Opt. Lett.* **36**(5), 597–599 (2011).
16. L. V. Wang, Ed., *Photoacoustic Imaging and Spectroscopy*, Taylor & Francis/CRC Press, Boca Raton, FL (2009).
17. G. Ku et al., "Multiple-bandwidth photoacoustic tomography," *Phys. Med. Biol.* **49**(7), 1329–1338 (2004).
18. B. Wang et al., "Detection of lipid in atherosclerotic vessels using ultrasound-guided spectroscopic intravascular photoacoustic imaging," *Opt. Express* **18**(5), 4889–4897 (2010).
19. B. Wang et al., "Intravascular photoacoustic imaging of lipid in atherosclerotic plaques in the presence of luminal blood," *Opt. Lett.* **37**(7), 1244–1246 (2012).
20. S. Sethuraman et al., "Spectroscopic intravascular photoacoustic imaging to differentiate atherosclerotic plaques," *Opt. Express* **16**(5), 3362–3367 (2008).
21. B. Wang et al., "Plasmonic intravascular photoacoustic imaging for detection of macrophages in atherosclerotic plaques," *Nano Lett.* **9**(6), 2212–2217 (2009).
22. X. Li et al., "80-MHz intravascular ultrasound transducer using PMN-PT free-standing film," *IEEE Trans. Ultrason. Ferroelectr. Freq. Control* **58**(11), 2281–2288 (2011).
23. B. Y. Hsieh et al., "Integrated intravascular ultrasound and photoacoustic imaging scan head," *Opt. Lett.* **35**(17), 2892–2894 (2010).
24. W. Wei et al., "Integrated ultrasound and photoacoustic probe for co-registered intravascular imaging," *J. Biomed. Opt.* **16**(10), 106001 (2011).
25. A. B. Karpouk, B. Wang, and S. Y. Emelianov, "Development of a catheter for combined intravascular ultrasound and photoacoustic imaging," *Rev. Sci. Instrum.* **81**(1), 014901 (2010).
26. P. J. Fitzgerald et al., "Intravascular ultrasound imaging of coronary arteries. is three layers the norm?," *Circulation* **86**(1), 154–158 (1992).
27. Z. Guo, L. Li, and L. V. Wang, "On the speckle-free nature of photoacoustic tomography," *Med. Phys.* **36**(9), 4084–4088 (2009).
28. S. L. Jacques and S. A. Prah, Oregon Medical Laser Center, "Optical properties spectra," <http://omlc.ogi.edu/spectra/> (19 September 2012).
29. F. S. Foster et al., "Ultrasound backscatter from blood in the 30 to 70 MHz frequency range," in *IEEE Ultrasonics Symp.*, Cannes, France, Vol. 3, pp. 1599–1602 (1994).